# Northeast Pacific Marine Heatwaves Driven by Seasonality of ENSO and Reemergence

**Tongtong Xu[1,2*], Sang-Ik Shin[1,2], Matthew Newman[2], Antonietta Capotondi[1,2], Daniel J. Vimont[3,4], Michael A. Alexander[2], and Emanuele Di Lorenzo[5],**

[1] CIRES, University of Colorado Boulder, CO.

[2] NOAA Physical Sciences Laboratory, CO.

[3] Nelson Institute Center for Climatic Research, University of Wisconsin–Madison, WI.

[4] Atmospheric and Oceanic Sciences Department, University of Wisconsin–Madison, WI.

[5] Department of Earth, Environmental, and Planetary Sciences, Brown University, RI.

Corresponding author: Tongtong Xu (tongtong.xu@noaa.gov)

## Abstract

Northeast Pacific Marine Heatwaves (MHWs) have widespread ecological and socioeconomic consequences that are sensitive to event duration and intensity. Using an empirical dynamical model capturing important seasonal cycle processes, we show that Northeast Pacific MHW event duration is linked to the seasonality of both the El Niño-Southern Oscillation (ENSO) lifecycle and North Pacific Ocean mixed layer physics, including subsurface storage and subsequent reemergence of the previous year's thermal anomalies. Long-lasting MHW and strong ENSO events tend to evolve in quadrature: As a MHW event that reaches peak intensity in late spring begins weakening in fall, its related subtropical surface anomalies strengthen El Niño, whose extratropical teleconnections in turn enhance MHW amplitude during winter. The following spring, reemergence of the previous year's warm surface temperatures can further prolong the event. In contrast, shorter but still potentially intense MHWs in spring and summer can be maintained by North Pacific internal dynamics alone.

150/150


## Introduction

Marine Heatwaves (MHWs) are prolonged periods of extreme sea surface temperature anomalies (SSTA) (Hobday et al. 2016) that occur in many regions of the global oceans (Frolicher & Laufkotter 2018; Holbrook et al. 2019; Oliver et al. 2021; Guo et al. 2022; Xu et al. 2022), causing extensive ecological disruptions and socioeconomic consequences (e.g., Smith et al. 2021; Smith et al. 2023 and the references therein). The Northeast Pacific Ocean, a well-recognized MHW hotspot, has recently experienced two extreme MHW events: "The Blob" (Bond et al. 2015), which developed during the boreal winter of 2013/14 and persisted into the following year (Fig. 1a), and "The Blob 2.0" (Amaya et al. 2020), primarily peaking in the boreal summer of 2019 (Fig. 1b). These events led to massive strandings and/or mortalities of sea lions, seals, seabirds, and marine invertebrates, as well as harmful algal blooms and commercial fishery closures (Smith et al. 2021; Smith et al. 2023). Understanding the physical drivers of Northeast Pacific MHWs is crucial for predicting and mitigating their adverse impacts on marine ecosystems.

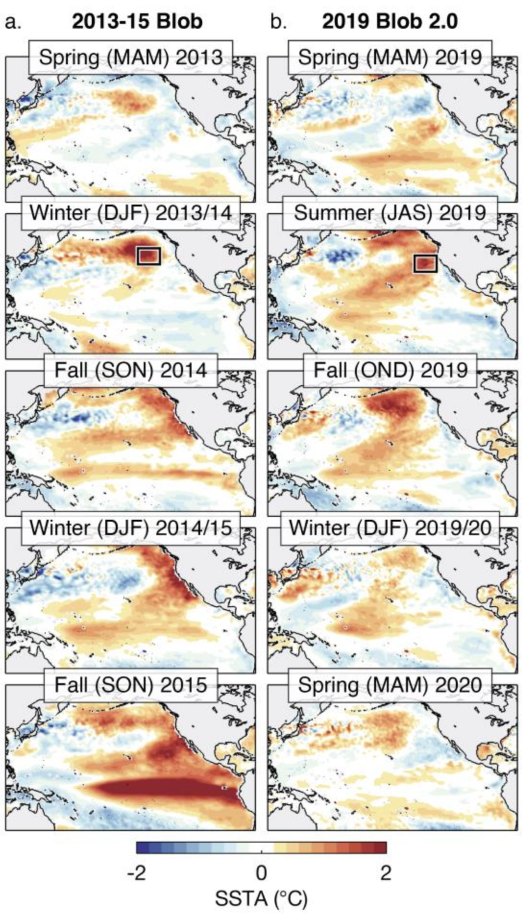


Figure 1. The two record-high Northeast Pacific Marine Heatwaves (MHWs) – the Blob and Blob 2.0. The life cycles of (a) the Blob during 2013-2015 and (b) Blob 2.0 during 2019 are shown as the evolution of observed seasonal SSTA Ocean Reanalysis System 5 (ORAS5; Zuo et al. 2019). Our results are not sensitive to the chosen datasets. Black boxes denote the representative region of the Blob (150$^{o}$W-135$^{o}$W; 35$^{o}$N-46$^{o}$N) and Blob 2.0 (140$^{o}$W-125$^{o}$W; 30$^{o}$N-41$^{o}$N). Acronym: March-April-May (MAM); December-

January-February (DJF); September-October-November (SON); July-August-September (JAS); October-November-December (OND).

The development of Northeast Pacific MHWs has been associated with both local and remote drivers. For example, intense MHWs are often associated with persistent atmospheric ridges that weaken surface wind speeds and their associated surface turbulent heat fluxes, leading to a reduction in oceanic heat loss and the formation of warm SSTA (Bond et al. 2015; Holbrook et al. 2019; Amaya et al. 2020; Sen Gupta et al. 2020). Large-scale Pacific climate variability can also modulate local drivers of the Northeast Pacific MHWs or create conditions favorable for their development. In particular, El Niño Southern Oscillation (ENSO) in the tropical Pacific has been estimated to drive about 20-40% of Northeast Pacific monthly SSTA variability (Zhao et al. 2021), and has been linked to the intensity, duration, and frequency of Northeast Pacific MHWs through both atmospheric and oceanic teleconnections (Di Lorenzo & Mantua 2016; Holbrook et al. 2019; Sen Gupta et al. 2020; Xu et al. 2021; Capotondi et al. 2022; Deser et al. 2024). However, since prolonged Northeast Pacific MHWs begin several months prior to the peak of ENSO events (e.g., Xu et al. 2021; Capotondi et al. 2022), MHW conditions may also be linked to the dynamics underpinning ENSO development. For example, Capotondi et al. (2022) found that a dynamical mode spanning the Northeast Pacific and the central equatorial Pacific (Barlow et al. 2001), which they termed the “NP-CP” mode, is important to both the development of Northeast Pacific MHWs and ENSO events. The NP-CP mode includes anomalies typical of the Pacific Meridional Mode (PMM; Chiang & Vimont 2004), a well-known ENSO precursor (Penland & Sardeshmukh 1995; Vimont et al. 2014; Capotondi & Sardeshmukh 2015). The PMM anomalies extend southwestward from the coast of California toward the central equatorial Pacific, where they can favor the development of a central Pacific El Niño (Vimont et al. 2014; Capotondi & Sardeshmukh 2015;

Amaya 2019). The NP-CP mode was previously identified as one component of the Pacific Decadal Oscillation (PDO; Newman et al. 2016), whose contribution to the development of Northeast Pacific MHWs has also been highlighted (Ren et al. 2023).

While key physical drivers of Northeast Pacific MHWs have been studied, less attention has been paid to the potentially important role of seasonality in MHW dynamics. For example, the seasonal variation of mixed layer depth impacts how rapidly the ocean warms or cools when forced by surface heat fluxes, and consequently the intensity of the resulting temperature anomalies. During summer, the shallow mixed layer (Kara et al. 2003) allows for more efficient oceanic heating, which can exacerbate MHW conditions (Scannell et al. 2020; Amaya et al. 2021; Chen et al. 2021; Shi et al. 2022; Takahashi et al. 2023). In contrast, although the deep oceanic mixed layer during winter can be expected to warm more slowly, it has greater memory. Additionally, when the mixed layer shoals in spring, anomalous heat can remain trapped beneath the mixed layer in the subsurface ocean and can “reemerge” at the surface in the following winter when the mixed layer deepens again, contributing to the development of SST anomalies (Alexander et al. 1999; Alexander et al. 2001; Scannell et al. 2020; Köhn et al. 2024). Moreover, the PMM is most pronounced in boreal spring (Amaya 2019; Meng & Li 2024), while ENSO tends to peak during boreal winter (Rasmusson & Carpenter 1982; Wang et al. 2017), likely making the influence of these modes on MHWs seasonally dependent. Finally, atmospheric variability in the extratropics exhibits considerable variation with the seasonal cycle, which can also translate to seasonally-varying forcing of MHWs (Johnstone & Mantua 2014).

In a previous study, Xu et al. (2021; X2021 hereafter) used a stationary Linear Inverse Model (LIM; Penland & Sardeshmukh 1995), a seasonally independent stochastically-forced multivariate empirical dynamical model constructed from monthly SSTA observations, to simulate a large number of Northeast Pacific MHWs of various intensity and duration. X2021 found that the duration of MHWs in the Northeast Pacific is related to ENSO development in the tropical Pacific, while MHW intensity is more likely linked to North Pacific internal variability. However, the LIM used by X2021 did not allow diagnostics of how seasonality impacts MHW development through tropical-extratropical interactions and internal North Pacific dynamics.

Here, we build upon X2021's earlier study by employing a Cyclostationary LIM (CS-LIM; Shin et al. 2021), which explicitly incorporates the seasonal dependence of both deterministic dynamics (Blumenthal 1991; von Storch et al. 1995; Johnson et al. 2000) and stochastic noise forcing of climate anomalies. The CS-LIM is constructed using monthly Pacific SSTA and sea surface height anomaly (SSHA) data for the years 1958-2021 from the Ocean Reanalysis System 5 (ORAS5; Zuo et al. 2019). SSHA was included to incorporate the impacts of upper ocean heat content on Pacific SSTA variability (Rebert et al. 1985; Capotondi et al. 2022; Zhang et al. 2024), which previous studies found to improve the simulation of both tropical-extratropical interactions (e.g. Newman et al. 2011b; Zhao et al. 2021) and ENSO diversity (Newman et al. 2011a; Capotondi & Sardeshmukh 2015). The use of a CS-LIM allows the representation of ENSO phase locking (Thompson & Battisti 2000; Xue et al. 2000; Kondrashov et al. 2005; Shin et al. 2021; Vimont et al. 2022), which, via tropical-extratropical interactions, could contribute to the seasonally varying behaviors of Northeast Pacific MHWs. We also find that this CS-LIM captures reemergence in the North Pacific, which has a strong seasonal dependence.

To diagnose the impact of the seasonality of the tropical-extratropical coupling as well as that associated with North Pacific internal ocean dynamics, we conduct two parallel decoupling experiments within the CS-LIM framework, removing the coupling between either (1) the tropical and North Pacific regions, or (2) North Pacific SSTA and SSHA. We find that the second experiment provides insights on the surface-upper ocean coupling, specifically revealing the role of reemergence processes. Our decoupling experiments are analogous to those conducted using coupled general circulation models (GCMs), where regional influences are investigated by prescribing climatological forcings (e.g., Frischknecht et al. 2015; Amaya et al. 2020) or by restoring certain regions to observations while allowing others to evolve freely (e.g., Deser et al. 2017; Amaya et al. 2019). See the Methods section for more details, illustrating how the CS-LIM experiments can be used similar to GCMs.

## Seasonal Variability of Northeast Pacific MHWs

We begin by examining the seasonal variability of the Northeast Pacific MHW region by constructing an index, termed "NEPac" index, from the spatially averaged monthly SSTA over an area that experiences large anomalies during MHWs (150$^o$W-135$^o$W, 35$^o$N-46$^o$N; black box in Fig. 1a; Xu et al. (2021)), for 1958-2021. The Probability Density Functions (PDFs) of the observed NEPac index differ substantially between the boreal winter and summer seasons (Fig. 2a-b). The width of the PDF is wider in summer than in winter, indicating that there were more extremes in summer than in winter (bars in Fig. 2a-b). The CS-LIM large ensemble, comprising 2000 realizations of possible alternative histories consistent with 1958-2021 statistics (see Methods), reproduces these seasonal differences well (thick black lines in Fig. 2a-b).

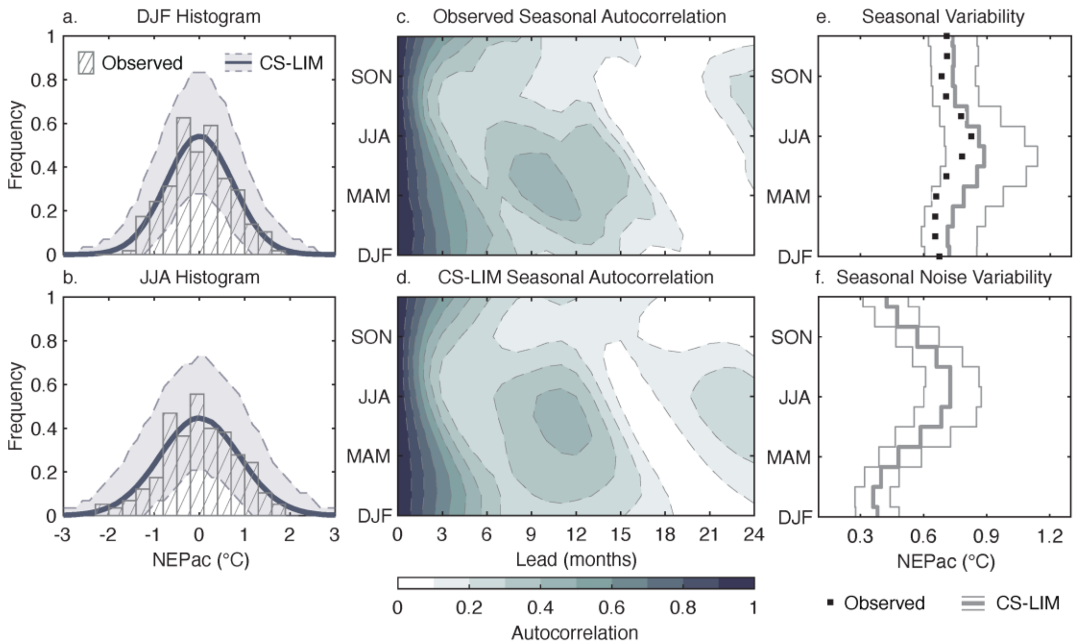


Figure 2. Seasonal variability of the Northeast Pacific MHW index (NEPac), as reproduced by the Cyclostationary Linear Inverse Model (CS-LIM). The NEPac index is obtained by spatially averaging SSTA within the region outlined by the black box in Fig. 1a. (a-b) Probability Density Functions (PDFs) of the observed (bars) and CS-LIM simulated NEPac indices (lines) for (a) winter (DJF) and (b) summer (JJA; June-July-August). (c-d) Seasonal autocorrelation of (c) the observed and (d) the CS-LIM simulated NEPac indices. The y-axis indicates the NEPac base season, and the x-axis shows the lead time; for example, the value plotted at (MAM, 6) represents the correlation between the NEPac value in MAM and its value six months later in SON. (e) Seasonal standard deviation of the observed (black squares) and the CS-LIM simulated NEPac indices (lines). (f) Seasonal standard deviation of the local noise forcing on the NEPac region simulated by CS-LIM (see Methods). The CS-LIM results are derived from 2000 realizations, from which the ensemble mean (shading in (d) and thick lines in (a-b, e-f)) and the 95% confidence interval (thin lines in (a-b, e-f)) of the PDFs, the autocorrelations, standard deviations are presented (see Methods).

Then we assessed the standard deviation of the NEPac index in each season as an indicator of seasonal variations in the width of the PDFs, and evaluated how well the observed seasonal variations are reproduced by the CS-LIM ensemble (Fig. 2e). The observed NEPac index has a higher standard deviation in summer and lower values during other seasons (black squares in Fig. 2e). The CS-LIM large ensemble generally reproduces this seasonal variability (lines in Fig. 2e), with the standard deviation peaking one month earlier than observed. However, this difference is not statistically significant. By construction, a stationary LIM (ST-LIM) ensemble of equivalent size, broadly similar to the model used by X2021, does not capture the observed annual cycle (Fig. S1).

For the CS-LIM to be useful for investigating MHW seasonality, it should also capture the seasonal variations of observed North Pacific mixed layer dynamics and its influence on SST. One way to evaluate this influence in the context of the CS-LIM is to compare the observed and the CS-LIM simulated autocorrelation between the NEPac index in a given season and the index in subsequent seasons (Fig. 2c-d). The longer (shorter) memory of SSTA associated with deeper (shallower) mixed layers during winter (summer) is illustrated by the decorrelation time scale, which is longer for winter anomalies compared to summer anomalies. While the correlation values generally decline with increasing lead times, they increase again in the fall (NDJ) and reach a secondary maximum during the following spring (FMA; February-March-April). This behavior results from the reemergence process (Alexander et al. 1999): As the mixed layer shoals in late spring, subsurface temperature anomalies that persist beneath the mixed layer through summer are subsequently re-entrained into the deepening mixed layer in the following fall. This process can also be seen in springtime NEPac index whose correlation with subsurface anomalies decreases in summer but then subsequently increases in fall (e.g., Newman et al. 2016; see also Fig. S2). Our CS-LIM appears to capture this behavior (Fig. 2d), albeit with a slight seasonal offset, as the peak correlation related to the reemergence mechanism occurs in April-May-June instead of FMA as in observations. In contrast, the ST-LIM shows no seasonal variations in the decorrelation time scale and does not exhibit reemergence signals (Fig. S3).

We also expect seasonal noise forcing variability due to seasonality of the net surface heat flux from the atmosphere and the varying mixed layer depth (i.e., heat capacity). In the CS-LIM, we assess the seasonal standard deviation of simulated local noise forcing imposed on the NEPac region (see Methods; Fig. 2f). The simulated local noise forcing displays a noticeable seasonal transition, with larger forcing in late summer (JAS) compared to other seasons. This is consistent with the seasonal variations of the net surface heat flux anomalies distributed over the seasonally varying mixed layer depth in the Northeast Pacific (Shi et al. 2022), suggesting that our CS-LIM is capable of representing the net effect of the noise forcing and is hence suitable for diagnosing the seasonality of MHWs.

MHWs were initially defined as anomalously warm events that last at least five days above the 90$^{th}$ percentile of the local SST (Hobday et al. 2016). This definition was chosen in analogy with land heatwaves and has recently been extended to account for longer-lasting events or persistent impacts on marine ecosystems (see reviews by Capotondi et al. 2024 and references therein). Some recent studies, starting with Scannell et al. (2016), have employed an intensity-duration-frequency (IDF) approach that determines the frequency of events for varying intensity and duration threshold pairs (Xu et al. 2021; Xu et al. 2022). This approach offers the advantage of defining MHWs as a class, representing a generalized method that can summarize events across a wide range of historical conditions. The resulting IDF plot for historical occurrences of Northeast Pacific MHWs over the 1958-2021 period (top row of Fig. 3a; see Methods) is similar to that previously found by X2021 using Extended Reconstruction SST, version 3 (ERSST.v3; Smith et al. 2008) data. For example, two standard deviation ($2\sigma$) events that lasted at least one month have occurred 1.56 times per decade. More generally, in the Northeast Pacific, MHWs that were extreme in intensity but dissipated rapidly and MHWs that were less intense but persisted over extended periods were equally likely to have occurred.

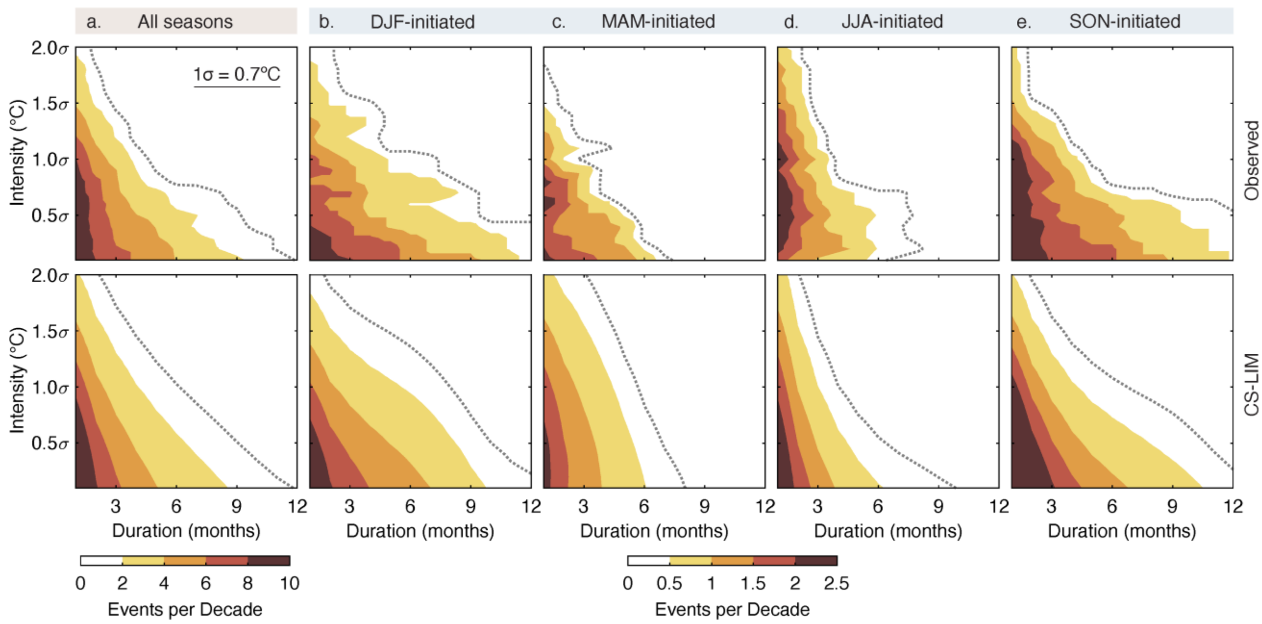


Figure 3. Intensity-Duration-Frequency (IDF) map of Northeast Pacific MHWs, categorized by the season in which they started. IDFs are derived from the NEPac index by calculating the number of events exceeding each intensity and duration threshold pair (see Methods). Events are categorized by their onset season: (a) all seasons, (b) winter-initiated (DJF), (c) spring-initiated (MAM), (d) summer-initiated (JJA), and (e) fall-initiated (SON). The top row shows the IDFs derived from the observed NEPac index, while the bottom row displays the ensemble mean statistics derived from the 2000 CS-LIM simulated NEPac indices. The dotted lines represent frequency contours of (a) 1 event per decade, (b-e) 0.25 event per decade. The difference between the bottom and top rows is insignificant (95% confidence interval of the simulated statistics; two-tailed). One standard deviation ($1\sigma$) of the NEPac index is $0.7^{o}$C.

We can further categorize MHW events based on their onset seasons (top row of Fig. 3b-e): How many events meeting given intensity and duration thresholds started in DJF (“winter-initiated”), MAM (“spring-initiated”), SON (“fall-initiated”), or JJA (“summer-initiated”)? The corresponding IDFs reveal that fall and winter-initiated events tend to have longer duration, whereas spring and summer-initiated events are more typically shorter-lived. Summer-initiated events are generally the most intense, followed by fall and winter-initiated events, with spring-initiated events being the weakest among all seasons. For example, historically, there were 10 events that exceeded the 2σ intensity threshold and lasted at least 1 month: 2 initiated in winter

(1963/02, 2014/01), 0 in spring, and 4 each in summer (1958/07, 1962/06, 1965/06, 1967/08) and fall (1959/11, 1991/10, 2019/11, 2020/11). In contrast, only 3 events exceeded the 1σ intensity threshold and lasted at least 6 months, all of which were winter-initiated (1962/01, 1965/02, 2015/02). Notably, the two Blob events display similar characteristics, with the first Blob appearing in winter and lasting for several months, while Blob 2.0 began in the summer and, although relatively short-lived, was very intense.

The CS-LIM large ensemble reproduces these MHW statistics, not only year-round as in X2021 but also when categorized by season (cf. bottom with top row of Fig. 3). Specifically, CS-LIM simulated events are more likely to have a longer duration when they are initiated in fall or winter than in spring or summer. They are also more likely to exhibit greater intensities when summer-initiated than when fall and winter-initiated. The only exception is spring-initiated events, where the CS-LIM simulates a stronger intensity than observed, which may be related to the early peak in the CS-LIM standard deviation compared to observations (Fig. 2e). Despite this, we find that there are no significant differences between IDF plots constructed from observations and those constructed from the CS-LIM ensembles. It is also worth noting that while our NEPac index primarily focuses on the key region of the Blob, our findings are qualitatively similar if we instead use an index representing the location of the Blob 2.0 (Fig. 1b and Fig. S4).

## Seasonal Evolution of Northeast Pacific MHWs

Since the CS-LIM can capture the seasonality of observed dynamics and noise forcing along with the observed frequencies of Northeast Pacific MHWs across different seasons, we use its large ensemble to diagnose how MHW evolution and its dynamics depend upon the seasonal cycle. We will focus our analysis on MHWs whose intensity exceeds the 1$\sigma$ (0.7 $^{o}$C) threshold, which allows us to target events of longer duration. However, the results are not qualitatively sensitive to this choice.

The impact of seasonality on MHW evolution within the CS-LIM ensemble is shown in Fig. 4, which displays the composite evolution of both the NEPac (contours) and Niño3.4 (shading) indices from 6 months prior to MHW onset to 24 months after, determined separately for each onset (or "initiated") season and different duration (3, 6, 9 & 12 months). For example, the horizontal lines labeled "DJF" on the y-axis represent the composite evolution of DJF-initiated MHWs, plotted from 6 months prior (i.e., JJA on the x-axis) to 24 months after (i.e., DJF on the x-axis) the onset. In this way, consistent signals in the vertical suggest seasonal phase-locking, whereas slanted signals indicate lead/lag behaviors relative to the onset.

We find that MHWs become increasingly phase-locked as the duration of the events increases. As event duration exceeds 12 months (Fig. 4d), the MHWs tend to consistently peak near boreal summer (i.e., JJA), the season of highest standard deviation (Fig. 2e), no matter when the event was initiated. Some phase locking is also noticeable for events lasting $\geq$ 9 months, but only weakly present for events lasting $\geq$ 6 months. Note also that there appears to be reemergence of MHW amplitudes occurring several months after the primary events, which also appears to be somewhat independent of initiation season (and lead time) since it typically occurs in boreal spring (MAM), persisting into summer (JAS). This is best illustrated by MHWs lasting $\geq$ 6 months, where the primary and the secondary maxima are clearly separated, with second MHWs reemerging several months after the initial events fall below the intensity threshold. For MHWs lasting $\geq$ 9 or 12 months, the reemergence of those second MHWs becomes more pronounced, which, when the previous events do not weaken significantly, can lead to multiyear MHWs that do not fall below the intensity threshold until ~18-20 months after onset (e.g., in Fig. 4d, events initiated in DJF can persist until JAS in the following year).

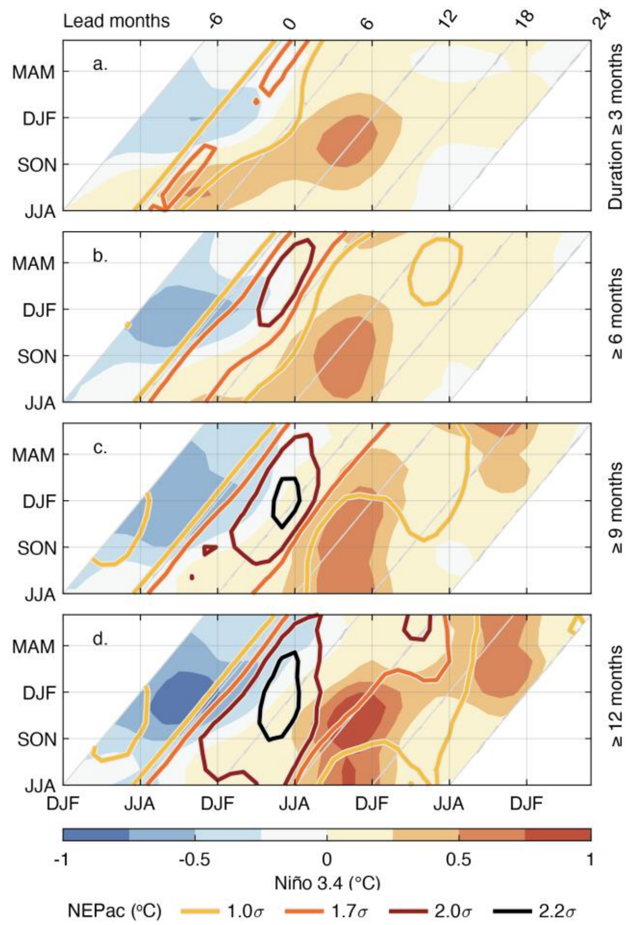


Figure 4. The composite evolution of CS-LIM simulated Northeast Pacific MHWs, initiated in different seasons and persisting for various durations, as well as the concurrent evolution in the tropical Pacific. Contours denote the evolution of Northeast Pacific MHWs, indicated by the NEPac index at contour levels of $1.0\sigma$, $1.7\sigma$, $2.0\sigma$ and $2.2\sigma$ °C. These contour levels are chosen to capture the key features (e.g., the peak intensity) of MHW evolution with only a few levels. The shading denotes the concurrent evolution in the tropical Pacific, indicated by the Niño 3.4 index. Diagonal gray lines indicate the lead/lag months relative to the onset of MHWs (at 0 lead month), spanning from 6 months prior to 24 months after the onset. The y-axis marks the onset seasons of MHWs, corresponding to the 0-month diagonal line. The x-axis marks the seasons during the MHW evolution. Each panel differs only in terms of the duration of MHWs, with panels (a-d) showing MHWs that stay above the $1\sigma$ intensity for at least 3, 6, 9, and 12 months, respectively.

In the tropical Pacific, the Niño3.4 region (shading of Fig. 4) typically exhibits weak cooling conditions prior to MHW onset, with stronger cooling associated with longer duration MHWs. Then, as the MHW develops and intensifies, the tropics transition into El Niño-like conditions, with the warm anomaly peaking after the MHWs reach their maximum intensity. That is, Niño 3.4 and the NEPac index evolve roughly in quadrature, especially for longer-duration events. These MHW/ENSO evolution aspects are generally consistent with X2021's findings using a stationary LIM. The CS-LIM additionally shows that El Niño is seasonally phase-locked and peaks near the start of winter (NDJ), consistent with previous studies (e.g., Shin et al. 2021; Vimont et al. 2022).

Overall, MHW phase locking in the Northeast Pacific is more pronounced for long-duration events, while shorter events tend to peak at similar lead times after onset. Moreover, differences in MHW onset season and duration are related to both the development and timing of ENSO events. For example, short-duration MHWs (Fig. 4a) in the warmer seasons (between March and November) would more likely lead to stronger intensities 1-2 months after onset, whereas events initiated in boreal winter (between December and February) tend to be weaker. However, with increasing MHW durations (Figs. 4c-d), this changes so that the strongest MHW events tend to be those initiated in the boreal fall and winter. Additionally, although peak ENSO conditions are phase-locked to early winter, their timing can range from 12 to 20 months after MHW onset, with winter-initiated MHWs leading to the earliest ENSO peaks and spring-initiated ones leading to the latest.

## Impact of remote tropics and internal North Pacific processes

In this section, we examine the relative role of remote tropical influences and internal North Pacific processes in the Northeast Pacific variability and MHWs. We start by evaluating how these dynamical processes impact the overall statistics of the NEPac index, and then explore in more detail how these processes impact Northeast Pacific MHW evolution.

First, we examine the CS-LIM ensembles (2000 realizations of 64-yr segments) that were rerun with either the tropical-extratropical or North Pacific SSTA-SSHA coupling entirely removed (see Methods). When the tropical-extratropical coupling is removed, the autocorrelation of the simulated NEPac indices is almost unchanged compared to the original CS-LIM ensemble (cf. Fig. 5a with Fig. 2d); if anything, the reemergence signals appear to be slightly strengthened. The standard deviation is also minimally affected (cf. brown lines with gray lines in Fig. 5b). The limited influence of tropical-extratropical coupling on the NEPac region might be linked to its location straddling a node of the PDO pattern (not shown but see Zhao et al. 2021), even though this coupling has a widespread impact on SSTA variance in the North Pacific, particularly enhancing PDO amplitude.

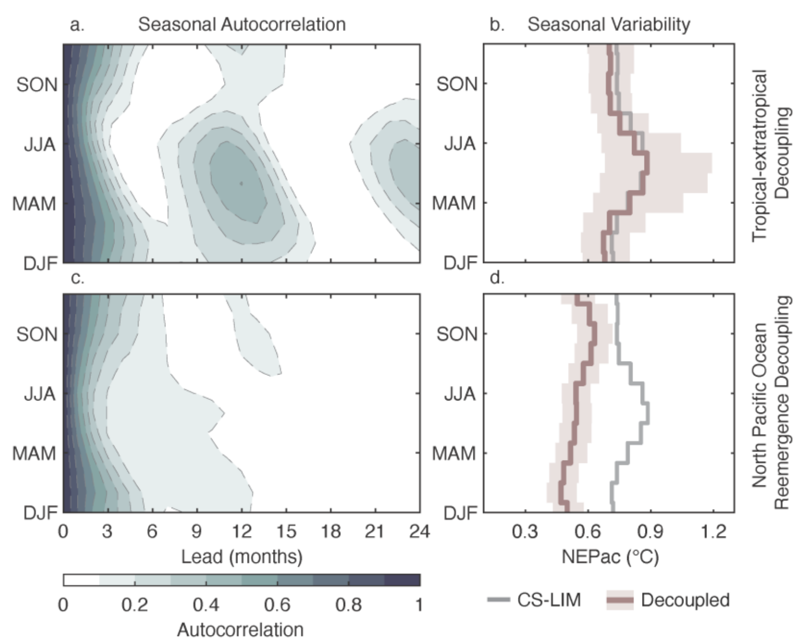


Figure 5. Seasonal variability of the CS-LIM simulated NEPac indices after removing (a-b) the tropical-extratropical coupling or (c-d) the North Pacific Ocean reemergence effect. (a, c) Seasonal autocorrelation

and (b, d) seasonal standard deviation (mean: thick brown line; shading: 95% confidence interval), derived from 2000 realizations of the respective decoupled simulations. The gray line in (b, d) is identical to that in Fig. 2e, representing the seasonal standard deviation of the simulated NEPac indices from the fully-coupled CS-LIM.

When North Pacific SSTA and SSHA are decoupled in the CS-LIM, we find that the NEPac autocorrelation function (Fig. 5c) loses the reemergence structure that is seen in both observations and the fully coupled CS-LIM ensemble (Figs. 2b and e). This supports our earlier inference that including SSHA in addition to SSTA in the CS-LIM allows us to capture reemergence, and decoupling SSTA from SSHA removes this process. This result can be understood in terms of the dynamical association between SSHAs and upper-ocean heat content (Deser et al. 2003; Capotondi et al. 2023; Zhang et al. 2024; see also Fig. S5), with high heat content values implying the presence of subsurface temperature anomalies that can be re-entrained into the mixed layer during its deepening phase. We also find that this reemergence process, which lengthens effective SSTA decorrelation time scales, significantly increases SSTA variance through most of the year (Fig. 5d).

We next examine the MHW statistics in the two decoupled ensembles, and compare them to those in the fully-coupled CS-LIM ensemble (Fig. 6). We find that the changes in MHW statistics appear to be consistent with the differences in variability between the decoupled and the fully coupled ensembles. For example, similar to the somewhat strengthened reemergence signals in the tropical-extratropical decoupled experiment (Fig. 5a), the IDFs also show increased occurrences of MHWs initiated in boreal spring (top row of Fig. 6b). MHWs initiated in other seasons have much smaller changes (top row of Fig. 6a, c, d), consistent with the almost unchanged standard deviations (Fig. 5b).

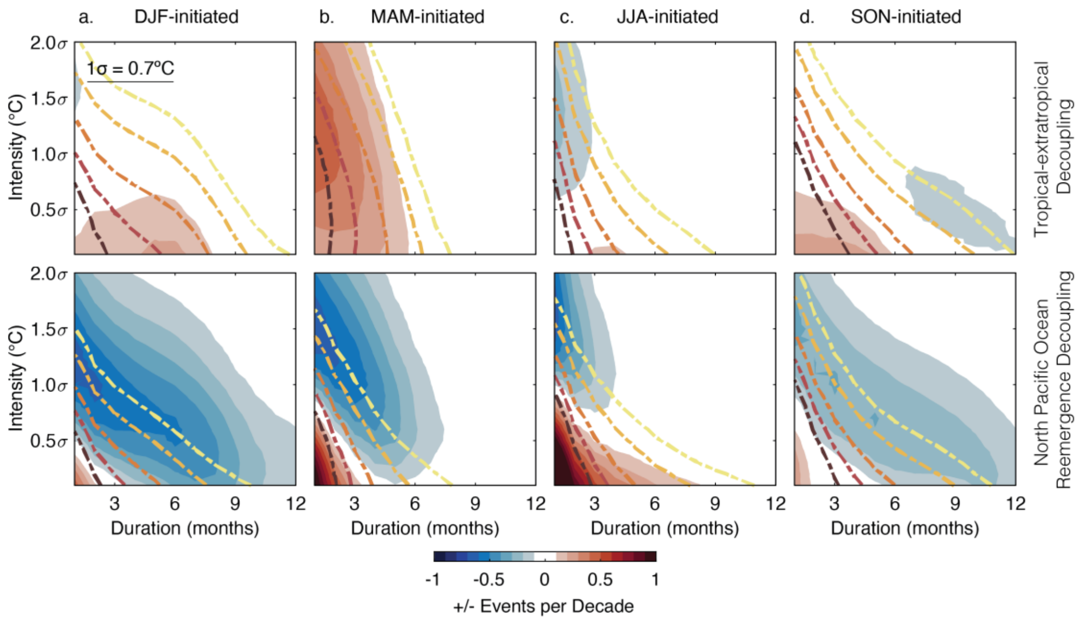


Figure 6. Seasonal IDF map of the CS-LIM simulated NEPac indices after removing (top row) the tropical-extratropical coupling or (bottom row) the North Pacific Ocean reemergence effect. Dashed-dotted lines denote the IDF map at contour levels of 0.25, 0.5, 1, 1.5 and 2 events per decade, matching the dotted lines and the shading interval in Fig. 3. Shading represents the changes in IDFs between the respective decoupled (contours) and the fully-coupled simulations (bottom row of Fig. 3). Negative (positive) changes indicate decreases (increases) in the MHW occurrences after decoupling. Each column differs only in terms of the onset seasons: (a) DJF-initiated, (c) MAM-initiated, (d) JJA-initiated, and (e) SON-initiated.

In contrast, when North Pacific SSTA and SSHA are decoupled, the occurrences of MHWs with high intensity, or both high intensity and long duration, decrease substantially (bottom row of Fig. 6), reflecting the markedly reduced variance (Fig. 5d). Conversely, mild events, especially those with short durations, tend to increase. This increase in mild events also reflects the decreased occurrences of intense MHWs as, by definition, MHWs that no longer qualify as intense would instead be classified as weak events.

Next, we conduct restart experiments to diagnose how these coupling dynamics drive the evolution of individual MHWs by restarting each MHW in the fully-coupled CS-LIM ensemble either from its onset or from 6 months before the onset but removing the tropics or SSH coupling during the subsequent evolution (Figs. 7 and 8). Note that this approach differs from the experiments used to produce Figs. 5 and 6, where the coupling was removed from the entire simulation. While the previous experiments allow us to examine the overall statistical changes after decoupling (and hence does not simulate the same MHWs as the fully coupled simulation), the restart experiments focus on understanding how turning off specific dynamics during the MHW evolution alters the progression of individual events.

We find that removing the tropical-extratropical coupling from MHW onset onward (Fig. 7a-d) results in only minor changes in MHW evolution, especially for the events with pronounced early summer peaks that typically begin in late fall and winter. Consistent with X2021's earlier results, tropical-North Pacific coupling primarily extends the duration of MHWs. This effect is most notable for events that are initiated between March and September, which have decreasing amplitudes during the subsequent fall and winter, when the events would otherwise have persisted under the influence of tropical-extratropical coupling. When this tropical effect is strong enough to maintain MHW amplitude above the onset threshold amplitude, the event has enhanced duration rather than appearing as two separate, shorter duration events. Consistent with Fig. 4a, the tropical effect is not particularly apparent for MHWs with short (e.g., 3 months) duration. More generally, note that despite weaker amplitudes and likely shorter durations, the primary evolution of MHWs since onset, along with those secondary peaks that begin in boreal spring and persist into summer, does not fundamentally change, suggesting a more important role for internal North Pacific dynamics. This is also consistent with X2021, who suggested that the intensity of Northeast Pacific MHWs may be primarily driven by variability intrinsic to the extratropics.

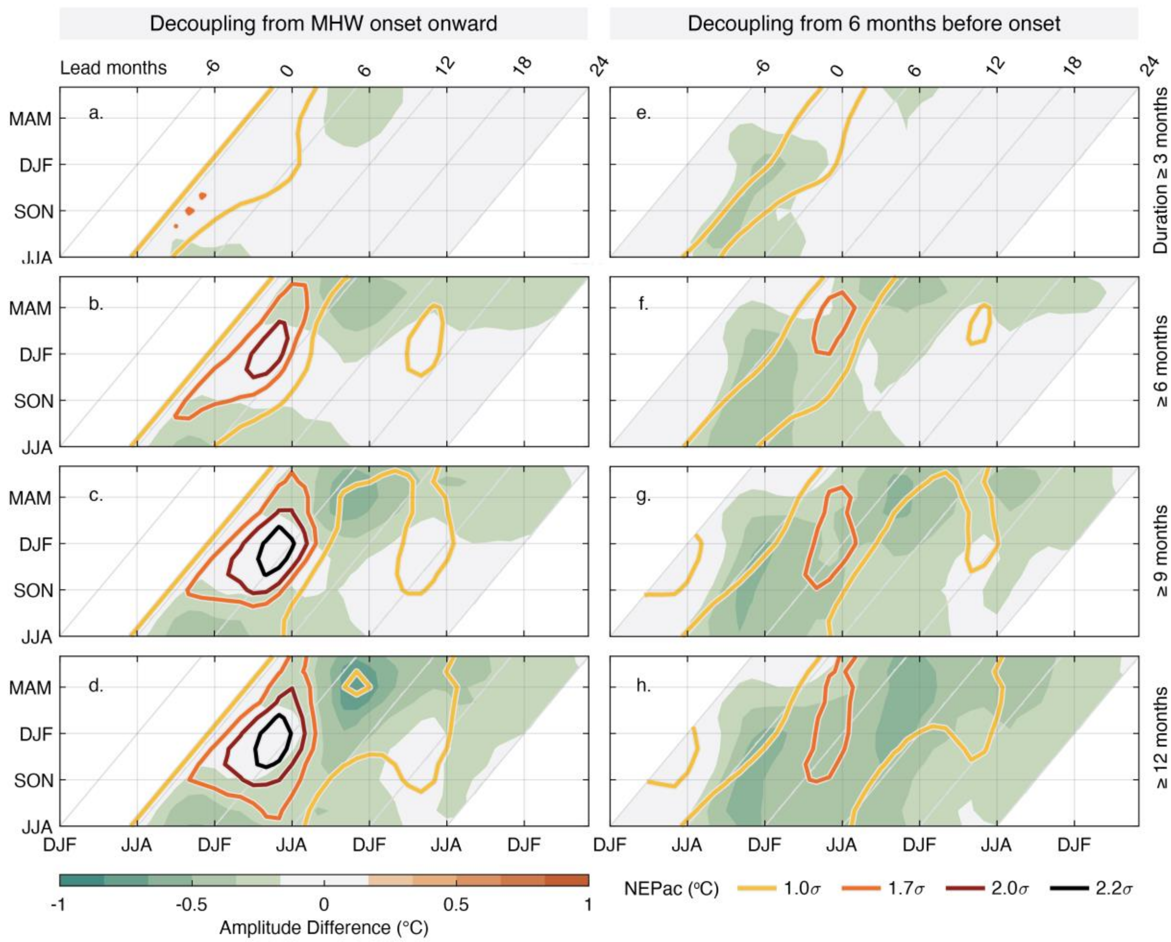


Figure 7. The remaining composite evolution of CS-LIM simulated Northeast Pacific MHWs, initiated in different seasons and persisting for various durations, after removing tropical-extratropical coupling (see Methods). The coupling is removed (a-d) starting from MHW onset or (e-h) starting 6 months prior to MHW onset. Contours denote the composite evolution of Northeast Pacific MHWs without the coupling effect. Shading indicates the difference in MHW evolution with (contours in Fig. 4) and without (contours) the coupling effect. Negative (positive) amplitude differences represent decreases (increases) in amplitude due to the absence of the coupling effect. Other configurations are the same as in Fig. 4.

When the tropical-extratropical coupling is removed starting 6 months before MHW onset (Fig. 7e-h), our results highlight the importance of precursor conditions favorable for MHW onset. The preferred precursors may include weak cooling conditions in the tropical Pacific and weak warming in the Northeast Pacific (Fig. 4 and Fig. S6). The weak cooling precondition is more evident for MHWs initiated in boreal winter (Fig. 4), whereas it is generally weaker in other seasons. Removing these preconditions several months before MHW onset would weaken MHW amplitudes (Fig. 7e-h). Conversely, retaining these preconditions until MHW onsets would preserve the subsequent growth and evolution of MHWs, even after removing tropical-extratropical coupling from onset onward (Fig. 7a-d).

When the coupling between North Pacific SSTA and SSHA is removed from MHW onset onward (Fig. 8a-d), the effect of reemergence also appears to be removed. Consequently, the MHW amplitude is considerably weaker, especially during spring and early summer, regardless of onset season and duration. Additionally, while the original second MHWs disappear, MHWs initialized in boreal spring tend to have lingering anomalies that appear as second MHWs in the fall and winter. Overall, the substantially weakened and shortened MHWs after decoupling North Pacific SSTA from SSHA highlight the importance of North Pacific mixed layer dynamics, in line with a previous study indicating the key role of initial SSHAs for MHW growth (Capotondi et al. 2022).

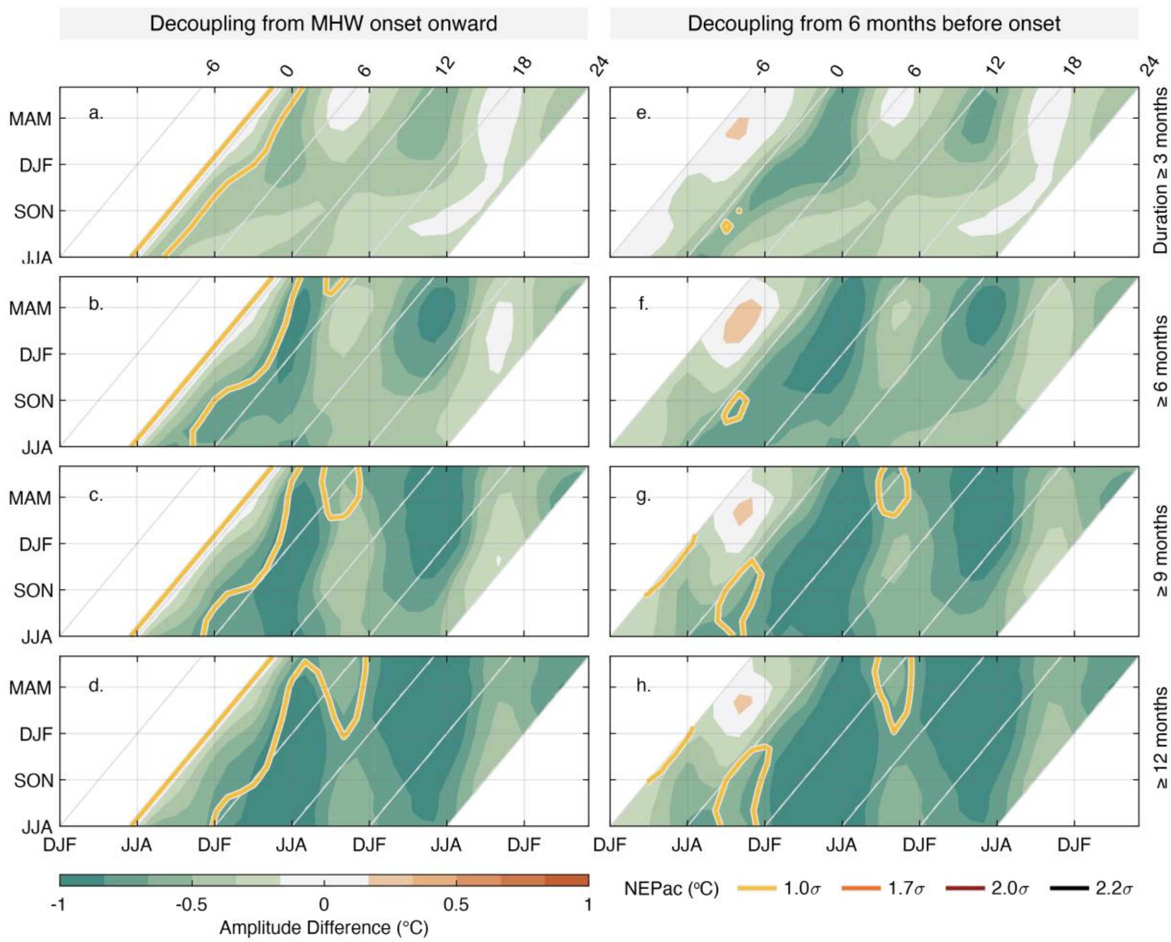


Figure 8. The same as Fig. 7, except that the North Pacific Ocean reemergence is removed (a-d) starting from MHW onset or (e-h) starting 6 months prior to MHW onset.

MHWs can be further weakened and almost entirely disappear when the decoupling is applied starting 6 months before the onset (Fig. 8e-h). Compared to decoupling from onset onward (Fig. 8a-d), this suggests that the upper ocean provides thermal inertia after MHW onset, such that once the Northeast Pacific reaches the MHW intensity threshold, it is likely to persist for some time before falling below the threshold.

## Discussion and Summary

In this study, we constructed a CS-LIM ensemble with 2000 realizations that reproduce the observed seasonal behavior of Northeast Pacific MHWs. The large number of simulated Northeast Pacific MHWs, compared to the small sample size in observations, allowed us to examine the statistics and composite evolution of MHWs initialized from any season and to analyze different seasonal aspects of the drivers leading to this evolution. We find that Northeast Pacific MHWs can clearly exhibit seasonally phase-locked evolution, reaching higher intensities in boreal summer and lower intensities in boreal winter, followed by the reemergence of second MHWs in the following spring and summer. This phase locking is more evident for long-lasting MHWs.

Tropical-extratropical coupling tends to contribute to the growth of Northeast Pacific MHWs in boreal fall and winter. Since the tropical Pacific does not usually reach peak El Niño conditions until the following fall and winter, this suggests that ENSO precursors may play a key role in the development and evolution of Northeast Pacific MHWs, corroborating the results of previous studies (Di Lorenzo & Mantua 2016; Capotondi et al. 2019; Amaya et al. 2020; Capotondi et al. 2022). We also analyze the role of the coupling between North Pacific SSTA and SSHA, finding its dominant contribution to both the primary peaks of MHWs in boreal summer and the secondary peaks reemerging in the following spring. Since SSHA is a reasonable indicator of upper ocean heat content (Rebert et al. 1985), our results highlight the significant role of internal North Pacific processes, suggesting a key role for entrainment of upper ocean warm anomalies through interactions with mixed layer depth variability. Note that this reemergence mechanism is in addition to the concurrent impact of seasonal variations of mixed layer depth on SSTAs that has been previously suggested as impacting MHW seasonality (Scannell et al. 2020; Amaya et al. 2021; Shi et al. 2022; Takahashi et al. 2023). Since reemergence provides year-to-year memory for

SSTAs, it also contributes to driving longer-lived MHWs. In summary, we highlight the importance of seasonality encapsulated in remote tropical and internal North Pacific dynamics on Northeast Pacific MHW evolution.

Our results have implications for the processes linked to the onset and persistence of Northeast Pacific MHWs. While weak cooling conditions in the tropical Pacific may not directly induce MHWs, they may favor conditions conducive to the formation of a higher-than-normal pressure system in the Northeast Pacific (Schwing et al. 2002), which is a recognized precursor for MHW onset (Bond et al. 2015). Once MHWs begin, North Pacific internal processes play a crucial role in driving MHWs and facilitating the development of central Pacific El Niño through mechanisms like seasonal footprinting (Vimont et al. 2003), meridional modes (Chiang & Vimont 2004; Vimont et al. 2014), and NP-CP modes (Capotondi et al. 2022), which are interrelated to some extent. The resulting El Niño conditions can, in turn, contribute to Northeast Pacific warming, particularly along the coast of North America, thereby extending the duration of MHWs. The reemergence of MHWs in the spring of the second year leads to a warmer ocean surface that may reduce low-cloud fraction, which, through positive low-cloud feedback, can prolong the persistence of these re-emerged warm anomalies into the summer (Ronca & Battisti 1997; Norris et al. 1998; Park et al. 2006; Myers et al. 2018; Schmeisser et al. 2019).

Lastly, while our MHW analyses suggest that incorporating SSHA in our CS-LIM framework implicitly provides information about North Pacific upper ocean dynamics, including mixed layer variability, SSHA ultimately serves as a proxy for pycnocline variability. Future studies will explore whether the use of alternative subsurface variables could further improve the results. Additionally, while the role of atmospheric variability in MHW onset and persistence is implicitly included, explicitly incorporating atmospheric variables could allow us to examine how their seasonal variations drive MHWs. These aspects will be the focus of investigation in a follow-up study.

## Methods

*Data*

Monthly SST and Sea Surface Height (SSH) at $1^o \times 1^o$ spatial resolution were obtained from the European Centre for Medium-Range Weather Forecasting (ECMWF) Ocean Reanalysis System 5 (ORAS5; Zuo et al. 2019) for the tropical and sea-ice free North Pacific regions ($25^o$S-$70^o$N, $120^o$E-$70^o$W) during the years 1958-2021. Anomalies of each field (SSTA, SSHA) were derived by removing the mean seasonal cycle and then removing the long-term trend identified by the ST-LIM (e.g., Frankignoul et al. 2017; Xu et al. 2022), which captures the accelerated trend over the historical period in many regions of the global ocean (Xu et al. 2022; Hemming et al. 2024). Empirical Orthogonal Functions (EOFs), representing the dominant patterns of variability, and the Principal Components (PCs), representing the time-evolving amplitudes of these patterns, were identified for sub-domains of each field, including tropical Pacific ($25^o$S-$25^o$N) and North Pacific ($25^o$N-$70^o$N). The leading 12/12 (8/8) PCs of SSTA/SSHA in the North Pacific (tropical Pacific) ocean were used for constructing the empirical framework, which explains 72.0%/50.7% (74.7%/66.7%) of the total variance in each field. This combination of PCs was chosen to realistically represent the variability while producing reasonably skillful hindcast of Northeast Pacific MHWs. Our results were not sensitive to this choice.

*Linear Inverse Model*

*a. Overview*

A linear dynamical system can reasonably approximate the evolution of ocean surface anomalies in the Pacific sector as,

$$\frac{\mathrm{d}\mathbf{x}}{\mathrm{d}t} = \mathbf{L}\mathbf{x} + \boldsymbol{\xi} \tag{1}$$

where $t$ is time, $\mathbf{x}(t)$ is the state vector, $\mathbf{L}$ is the linear dynamical operator that provides the deterministic evolution of the system, and $\boldsymbol{\xi}(t)$ is the stochastically-forced white noise (with spatial coherence), representing unpredictable and rapidly decorrelating nonlinearities (Penland & Sardeshmukh 1995; Shin et al. 2021; Xu et al. 2021; Zhao et al. 2021; Alexander et al. 2022; Capotondi et al. 2022; Xu et al. 2022). The general fluctuation-dissipation relation (FDR), also known as the Lyapunov equation governing the stability of such a linear dynamical system, is as follows:

$$\frac{\mathrm{d}\mathbf{C}(0)}{\mathrm{d}t} = \mathbf{L}\mathbf{C}(0) + \mathbf{C}(0)(\mathbf{L})^{\mathrm{T}} + \mathbf{Q} \tag{2}$$

in which $\mathbf{C}(0) = \langle \mathbf{x}(t)\mathbf{x}(t)^{\mathrm{T}} \rangle$ is the auto-covariance matrix, and $\mathbf{Q} = \langle \boldsymbol{\xi}(t)\boldsymbol{\xi}(t)^{\mathrm{T}} \rangle$ is the stochastic forcing covariance.

In a cyclostationary assumption, the first and the second statistical moments of $\mathbf{x}$ are cyclic with a period $T$. To incorporate the prominent annual cycle dependence of the climate system ($T$ = 12 months), CS-LIM determines $\mathbf{L}_j$ for each calendar month $j$ separately:

$$\mathbf{L}_j = \tau_0^{-1} \ln\left[\mathbf{C}_j(\tau_0)\mathbf{C}_j(0)^{-1}\right], \qquad j = 1,2,\dots,12 \tag{3}$$

where $\mathbf{C}_j(0) = \langle \mathbf{x}_j(t)\mathbf{x}_j(t)^{\mathrm{T}} \rangle$ and $\mathbf{C}(\tau_0) = \langle \mathbf{x}_j(t+\tau_0)\mathbf{x}_j(t)^{\mathrm{T}} \rangle$ are the lag-0 and the lag- $\tau_0$ covariance matrices, respectively. Note that $\tau_0$ is the training lag; here we used $\tau_0 = 1$ month following previous studies (e.g., Shin et al. 2021; Wang et al. 2023). Additionally, we use 3-month running means of the lag-0 and lag-$\tau_0$ covariance matrices centered on each calendar month before estimating $\mathbf{L}_j$, to effectively increase the sample size while retaining the seasonal cycle.

Having obtained $\mathbf{L}_j$, $\mathbf{Q}_j$ can be estimated via a discretized form of (2),

$$\frac{1}{2}\left[\mathbf{C}_{j+1}(0) - \mathbf{C}_{j-1}(0)\right] = \mathbf{L}_j\mathbf{C}_j(0) + \mathbf{C}_j(0)\left(\mathbf{L}_j\right)^{\mathrm{T}} + \mathbf{Q}_j, \quad j = 1,2, \dots, 12 \tag{4}$$

Note that $\mathbf{C}_j(0) = \mathbf{C}_{j+T}(0)$. See Shin et al. (2021) for detailed information on CS-LIM.

*b.* *Numerical Integration*

Following Penland & Matrosova (1994) and Shin et al. (2021), we numerically integrated the CS-LIM forward with a time step $\Delta t = 16\ hrs$,

$$\mathbf{y}(t + \Delta t) = [\mathbf{I} + \mathbf{L}\Delta t]\mathbf{y}(t) + \sqrt{\Delta t}\mathbf{S}\mathbf{r}(t) \tag{5}$$

$$\mathbf{x}(t + \Delta t/2) = [\mathbf{y}(t + \Delta t) + \mathbf{y}(t)]/2$$

where $\mathbf{S} = \mathbf{V}\sqrt{\mathbf{\Lambda}}$ is the stochastic forcing amplitude matrix ($\mathbf{V}$ and $\mathbf{\Lambda}$ are the eigenvectors and eigenvalues of $\mathbf{Q}$, respectively). $\mathbf{r}(t)$ is a random Gaussian noise vector whose components have zero mean and unit variance. Note that $\mathbf{L}$ and $\mathbf{S}$ exhibit periodic behaviours derived from (3) and (4). The numerical simulation, first initialized from $\mathbf{x}(0) = \mathbf{y}(0) = 0$ and ran for a 2000-yr spin-up time, were integrated for 128,000 yrs and divided into 2000-member ensembles of 64-yr segments matching the length of the observed record.

*c.* *Diagnostic Experimental Design*

Following previous studies such as Newman (2007), Zhang et al. (2021), Zhao et al. (2021), Alexander et al. (2022), Jin et al. (2023), and Kido et al. (2023), the coupled system between the tropical and North Pacific ocean basins can be expressed by rewriting (1) as,

$$\frac{\mathrm{d}}{\mathrm{d}t}\begin{bmatrix}\mathbf{x}_N\\ \mathbf{x}_T\end{bmatrix} = \begin{bmatrix}\mathbf{L}_{NN} & \mathbf{L}_{NT}\\ \mathbf{L}_{TN} & \mathbf{L}_{TT}\end{bmatrix}\begin{bmatrix}\mathbf{x}_N\\ \mathbf{x}_T\end{bmatrix} + \begin{bmatrix}\boldsymbol{\xi}_N\\ \boldsymbol{\xi}_T\end{bmatrix} \tag{6}$$

where the subscripts *N* and *T* represent the North Pacific and tropical Pacific fields, respectively. The submatrices of $\mathbf{L}$ encapsulate internal North Pacific ($\mathbf{L}_{NN}$) and tropical Pacific ($\mathbf{L}_{TT}$) processes, as well as the influence of the tropical Pacific (North Pacific) on the North Pacific (tropical Pacific), denoted by $\mathbf{L}_{NT}$ ($\mathbf{L}_{TN}$). The latter two terms are also referred to as the tropical-extratropical coupling dynamics. From (6), the North Pacific dynamical system can be separately written as,

$$\frac{\mathrm{d}\mathbf{x}_N}{\mathrm{d}t} = \mathbf{L}_{NN}\mathbf{x}_N + \mathbf{L}_{NT}\mathbf{x}_T + \boldsymbol{\xi}_N \tag{7}$$

Since the state vector $\mathbf{x}_N$ and $\mathbf{x}_T$ each includes SSTA and SSHA for the corresponding ocean basins, the internal North Pacific dynamics $\mathbf{L}_{NN}$ can be further decomposed as follows:

$$\mathbf{L}_{NN} = \begin{bmatrix}\mathbf{L}_{N,SST-N,SST} & \mathbf{L}_{N,SST-N,SSH}\\ \mathbf{L}_{N,SSH-N,SST} & \mathbf{L}_{N,SSH-N,SSH}\end{bmatrix} \tag{8}$$

Given that SSHA is a proxy for upper ocean heat content, these submatrices represent surface ($\mathbf{L}_{NSST-NSST}$) and upper ocean dynamics ($\mathbf{L}_{NSSH-NSSH}$), as well as their coupling ($\mathbf{L}_{NSST-NSSH}$ and $\mathbf{L}_{NSSH-NSST}$).

We conduct two decoupling experiments to diagnose different aspects of MHWs in the Northeast Pacific.

(1) We eliminate the coupling effect between the North Pacific and the tropical Pacific by setting $\mathbf{L}_{NT} = \mathbf{L}_{TN} = 0$, thereby isolating the dynamical system with processes internal to each ocean basin.

(2) We remove the coupling effect between North Pacific SSTA and SSHA by setting $\mathbf{L}_{N,SST-N,SSH} = \mathbf{L}_{N,SSH-N,SST} = 0$, hence allowing the surface ocean and upper ocean of the North Pacific to evolve independently.

For each experiment, we either rerun the entire CS-LIM ensemble (2000 realizations of 64-yr segments) without coupling dynamics, or restart each MHW in the fully-coupled CS-LIM ensemble, removing the coupling dynamics starting either from the MHW onset or 6 months before its onset, while keeping the Gaussian noise realization identical to the original CS-LIM integration. This allows us to diagnose the deterministic coupling effect on MHWs.

We note that the second experiment requires careful handling. Allowing the surface and upper oceans of the North Pacific to evolve independently can lead to changes in the tropical Pacific, which ultimately feed back to the North Pacific. As such, the result of experiment (2) would represent not only the coupling effect between SSTA and SSHA, but also the response and feedback from the tropical Pacific to that coupling effect. To avoid these additional changes, we adopt an approach similar to a pacemaker experiment (e.g., Deser et al. 2017; Amaya et al. 2019), by restoring the tropical Pacific evolution to be the same as in the original CS-LIM integration, while allowing the North Pacific to evolve freely under our specified diagnostic scenario.

*Intensity-Duration-Frequency (IDF) of MHWs*

Frequency is determined by calculating the number of events that exceed (≥) a given intensity for a period longer than (≥) a specified duration, divided by the total number of years in the observational record and multiplied by ten years. Therefore, the unit for frequency is events per decade. The IDF plot is constructed by calculating the frequency for each combination of intensity and duration thresholds. This includes intensities ranging from $0.1\sigma$ to $2.0\sigma$ and durations from 1 to 12 months.

## *Significance Tests*

(a) Probability Distribution of the NEPac index

For each realization of the 2000-member CS-LIM ensemble, we obtain the simulated Blob index, extract either DJF or JJA anomalies, and calculate their corresponding PDF. In Fig. 2a-b, the mean and the 95% confidence interval (2.5$^{th}$, and 97.5$^{th}$ percentiles) of the PDFs are depicted by solid and dashed lines, respectively.

(b) Seasonal standard deviation of the NEPac index

We obtain the simulated Blob index for each realization of the 2000-member CS-LIM ensemble and calculate the seasonally varying standard deviations. In Fig. 2e, the mean, 2.5$^{th}$, and 97.5$^{th}$ percentiles of the standard deviations are depicted by gray lines.

(c) Seasonal standard deviation of the noise forcing on the NEPac region

For each realization of the 2000-member CS-LIM ensemble, we derive seasonally-varying dynamical operator and noise forcing from (3) and (4). The amplitude of the noise forcing for each calendar month at each grid point can be estimated by taking the square root of the diagonal elements of $\mathbf{EOF} \cdot \mathbf{Q}_j \cdot \mathbf{EOF}^{\mathrm{T}}$. The noise forcing acting on the NEPac region can be estimated by averaging within the NEPac region. In Fig. 2f, the mean, 2.5$^{th}$, and 97.5$^{th}$ percentiles of the standard deviations are depicted by gray lines.

(d) Occurrences of MHWs

Following a procedure similar to deriving the IDF plot for the observed Blob index, we obtain the simulated Blob index from each realization of the 2000-member CS-LIM ensemble and calculate the IDF plot for each index. The $2.5^{th}$ and $97.5^{th}$ percentiles of the IDF plot are then compared with the observed IDF to assess the significance. For a given intensity and duration, the observed frequency significantly differs from our CS-LIM simulated frequency if it surpasses the $97.5^{th}$ percentile or falls below the $2.5^{th}$ percentile (Fig. 3).

## Data Availability

The ORAS5 reanalysis is publicly available at https://cds.climate.copernicus.eu/cdsapp#!/dataset/reanalysis-oras5?tab=overview. The large CS-LIM ensemble is available by running the MATLAB code provided at https://github.com/Tongtong-Xu-PSL/CS-LIM or upon request.

## Code Availability

All analyses were performed using MATLAB. Codes can be accessed at https://github.com/Tongtong-Xu-PSL/CS-LIM.


## Acknowledgements

This work was supported by NOAA cooperative agreements NA17OAR4320101 and NA22OAR4320151.

## REFERENCES

Alexander, M. A., C. Deser, and M. S. Timlin, 1999: The reemergence of SST anomalies in the North Pacific Ocean. *Journal of Climate*, **12,** 2419-2433.

Alexander, M. A., M. S. Timlin, and J. D. Scott, 2001: Winter-to-winter recurrence of sea surface temperature, salinity and mixed layer depth anomalies. *Progress in Oceanography*, **49,** 41-61.

Alexander, M. A., S.-I. Shin, and D. S. Battisti, 2022: The Influence of the Trend, Basin Interactions, and Ocean Dynamics on Tropical Ocean Prediction. *Geophysical Research Letters*, **49,** e2021GL096120.

Amaya, D. J., 2019: The Pacific Meridional Mode and ENSO: a Review. *Current Climate Change Reports*, **5,** 296-307.

Amaya, D. J., A. J. Miller, S.-P. Xie, and Y. Kosaka, 2020: Physical drivers of the summer 2019 North Pacific marine heatwave. *Nature Communications*, **11,** 1903.

Amaya, D. J., Y. Kosaka, W. Y. Zhou, Y. Zhang, S. P. Xie, and A. J. Miller, 2019: The North Pacific Pacemaker Effect on Historical ENSO and Its Mechanisms. *Journal of Climate*, **32,** 7643-7661.

Amaya, D. J., M. A. Alexander, A. Capotondi, C. Deser, K. B. Karnauskas, A. J. Miller, and N. J. Mantua, 2021: Are Long-Term Changes in Mixed Layer Depth Influencing North Pacific Marine Heatwaves? *Bulletin of the American Meteorological Society*, **102,** S59-S66.

Barlow, M., S. Nigam, and E. H. Berbery, 2001: ENSO, Pacific Decadal Variability, and U.S. Summertime Precipitation, Drought, and Stream Flow. *Journal of Climate*, **14,** 2105-2128.

Blumenthal, M. B., 1991: Predictability of a Coupled Ocean Atmosphere Model. *Journal of Climate*, **4,** 766-784.

Bond, N. A., M. F. Cronin, H. Freeland, and N. Mantua, 2015: Causes and impacts of the 2014 warm anomaly in the NE Pacific. *Geophysical Research Letters*, **42,** 3414-3420.

Capotondi, A., and P. D. Sardeshmukh, 2015: Optimal precursors of different types of ENSO events. *Geophysical Research Letters*, **42,** 9952-9960.

Capotondi, A., M. Newman, T. Xu, and E. Di Lorenzo, 2022: An Optimal Precursor of Northeast Pacific Marine Heatwaves and Central Pacific El Niño Events. *Geophysical Research Letters*, **49,** e2021GL097350.

Capotondi, A., R. R. Rodrigues, A. Sen Gupta, and coauthors, 2024: A Global Overview of Marine Heatwaves in a Changing Climate. *Communications Earth & Environment*, **under revision**.

Capotondi, A., P. D. Sardeshmukh, E. Di Lorenzo, A. C. Subramanian, and A. J. Miller, 2019: Predictability of US West Coast Ocean Temperatures is not solely due to ENSO. *Scientific Reports*, **9,** 10.

Capotondi, A., and Coauthors, 2023: Mechanisms of tropical Pacific decadal variability. *Nature Reviews Earth & Environment*, **4,** 754-769.

Chen, Z., J. Shi, Q. Liu, H. Chen, and C. Li, 2021: A Persistent and Intense Marine Heatwave in the Northeast Pacific During 2019–2020. *Geophysical Research Letters*, **48,** e2021GL093239.

Chiang, J. C. H., and D. J. Vimont, 2004: Analogous Pacific and Atlantic meridional modes of tropical atmosphere-ocean variability. *Journal of Climate*, **17,** 4143-4158.

Deser, C., M. A. Alexander, and M. S. Timlin, 2003: Understanding the Persistence of Sea Surface Temperature Anomalies in Midlatitudes. *Journal of Climate*, **16,** 57-72.

Deser, C., I. R. Simpson, K. A. McKinnon, and A. S. Phillips, 2017: The Northern Hemisphere extratropical atmospheric circulation response to ENSO: How well do we know it and how do we evaluate models accordingly? *Journal of Climate*, **30,** 5059-5082.

Deser, C., A. S. Phillips, M. A. Alexander, D. J. Amaya, A. Capotondi, M. G. Jacox, and J. D. Scott, 2024: Future Changes in the Intensity and Duration of Marine Heat and Cold Waves: Insights from Coupled Model Initial-Condition Large Ensembles. *Journal of Climate*, **37,** 1877-1902.

Di Lorenzo, E., and N. Mantua, 2016: Multi-year persistence of the 2014/15 North Pacific marine heatwave. *Nat Clim Change*, **6,** 1042-+.

Frankignoul, C., G. Gastineau, and Y. O. Kwon, 2017: Estimation of the SST Response to Anthropogenic and External Forcing and Its Impact on the Atlantic Multidecadal Oscillation and the Pacific Decadal Oscillation. *Journal of Climate*, **30,** 9871-9895.

Frischknecht, M., M. Munnich, and N. Gruber, 2015: Remote versus local influence of ENSO on the California Current System. *Journal of Geophysical Research-Oceans*, **120,** 1353-1374.

Frolicher, T. L., and C. Laufkotter, 2018: Emerging risks from marine heat waves. *Nature Communications*, **9,** 4.

Guo, X., and Coauthors, 2022: Threat by marine heatwaves to adaptive large marine ecosystems in an eddy-resolving model. *Nat Clim Change*, **12,** 179-186.

Hemming, M., M. Roughan, and A. Schaeffer, 2024: Exploring multi-decadal time series of temperature extremes in Australian coastal waters. *Earth Syst. Sci. Data*, **16,** 887-901.

Hobday, A. J., and Coauthors, 2016: A hierarchical approach to defining marine heatwaves. *Progress in Oceanography*, **141,** 227-238.

Holbrook, N. J., and Coauthors, 2019: A global assessment of marine heatwaves and their drivers. *Nature Communications*, **10,** 13.

Jin, Y., X. Meng, L. Zhang, Y. Zhao, W. Cai, and L. Wu, 2023: The Indian Ocean Weakens the ENSO Spring Predictability Barrier: Role of the Indian Ocean Basin and Dipole Modes. *Journal of Climate*, **36,** 8331-8345.

Johnson, S. D., D. S. Battisti, and E. S. Sarachik, 2000: Seasonality in an empirically derived Markov model of tropical Pacific sea surface temperature anomalies. *Journal of Climate*, **13,** 3327-3335.

Johnstone, J. A., and N. J. Mantua, 2014: Atmospheric controls on northeast Pacific temperature variability and change, 1900–2012. *Proceedings of the National Academy of Sciences*, **111,** 14360-14365.

Kara, A. B., P. A. Rochford, and H. E. Hurlburt, 2003: Mixed layer depth variability over the global ocean. *Journal of Geophysical Research: Oceans*, **108**.

Kido, S., I. Richter, T. Tozuka, and P. Chang, 2023: Understanding the interplay between ENSO and related tropical SST variability using linear inverse models. *Climate Dynamics*, **61,** 1029-1048.

Köhn, E. E., M. Vogt, M. Münnich, and N. Gruber, 2024: On the Vertical Structure and Propagation of Marine Heatwaves in the Eastern Pacific. *Journal of Geophysical Research: Oceans*, **129,** e2023JC020063.

Kondrashov, D., S. Kravtsov, A. W. Robertson, and M. Ghil, 2005: A Hierarchy of Data-Based ENSO Models. *Journal of Climate*, **18,** 4425-4444.

Meng, Z., and T. Li, 2024: Why is the Pacific meridional mode most pronounced in boreal spring? *Climate Dynamics*, **62,** 459-471.

Myers, T. A., C. R. Mechoso, G. V. Cesana, M. J. DeFlorio, and D. E. Waliser, 2018: Cloud feedback key to marine heatwave off Baja California. *Geophysical Research Letters*, **45,** 4345-4352.

Newman, M., 2007: Interannual to decadal predictability of tropical and North Pacific sea surface temperatures. *Journal of Climate*, **20,** 2333-2356.

Newman, M., S. I. Shin, and M. A. Alexander, 2011a: Natural variation in ENSO flavors. *Geophysical Research Letters*, **38,** 7.

Newman, M., M. A. Alexander, and J. D. Scott, 2011b: An empirical model of tropical ocean dynamics. *Climate Dynamics*, **37,** 1823-1841.

Newman, M., and Coauthors, 2016: The Pacific Decadal Oscillation, Revisited. *Journal of Climate*, **29,** 4399-4427.

Norris, J. R., Y. Zhang, and J. M. Wallace, 1998: Role of Low Clouds in Summertime Atmosphere–Ocean Interactions over the North Pacific. *Journal of Climate*, **11,** 2482-2490.

Oliver, E. C. J., J. A. Benthuysen, S. Darmaraki, M. G. Donat, A. J. Hobday, N. J. Holbrook, R. W. Schlegel, and A. S. Gupta, 2021: Marine Heatwaves. *Annual Review of Marine Science*, **13,** null.

Park, S., M. A. Alexander, and C. Deser, 2006: The Impact of Cloud Radiative Feedback, Remote ENSO Forcing, and Entrainment on the Persistence of North Pacific Sea Surface Temperature Anomalies. *Journal of Climate*, **19,** 6243-6261.

Penland, C., and L. Matrosova, 1994: A Balance Condition for Stochastic Numerical-Models with Application to the El-Nino-Southern Oscillation. *Journal of Climate*, **7,** 1352-1372.

Penland, C., and P. D. Sardeshmukh, 1995: The Optimal-Growth of Tropical Sea-Surface Temperature Anomalies. *Journal of Climate*, **8,** 1999-2024.

Rasmusson, E. M., and T. H. Carpenter, 1982: Variations in Tropical Sea Surface Temperature and Surface Wind Fields Associated with the Southern Oscillation/El Niño. *Mon Weather Rev*, **110,** 354-384.

Rebert, J. P., J. R. Donguy, G. Eldin, and K. Wyrtki, 1985: Relations between sea level, thermocline depth, heat content, and dynamic height in the tropical Pacific Ocean. *Journal of Geophysical Research: Oceans*, **90,** 11719-11725.

Ren, X., W. Liu, A. Capotondi, D. J. Amaya, and N. J. Holbrook, 2023: The Pacific Decadal Oscillation modulated marine heatwaves in the Northeast Pacific during past decades. *Communications Earth & Environment*, **4,** 218.

Ronca, R. E., and D. S. Battisti, 1997: Anomalous Sea Surface Temperatures and Local Air–Sea Energy Exchange on Intraannual Timescales in the Northeastern Subtropical Pacific. *Journal of Climate*, **10,** 102-117.

Scannell, H. A., A. J. Pershing, M. A. Alexander, A. C. Thomas, and K. E. Mills, 2016: Frequency of marine heatwaves in the North Atlantic and North Pacific since 1950. *Geophysical Research Letters*, **43,** 2069-2076.

Scannell, H. A., G. C. Johnson, L. Thompson, J. M. Lyman, and S. C. Riser, 2020: Subsurface Evolution and Persistence of Marine Heatwaves in the Northeast Pacific. *Geophysical Research Letters*, **47,** e2020GL090548.

Schmeisser, L., N. A. Bond, S. A. Siedlecki, and T. P. Ackerman, 2019: The role of clouds and surface heat fluxes in the maintenance of the 2013–2016 Northeast Pacific marine heatwave. *Journal of Geophysical Research: Atmospheres*, **124,** 10772-10783.

Schwing, F. B., T. Murphree, L. deWitt, and P. M. Green, 2002: The evolution of oceanic and atmospheric anomalies in the northeast Pacific during the El Niño and La Niña events of 1995–2001. *Progress in Oceanography*, **54,** 459-491.

Sen Gupta, A., and Coauthors, 2020: Drivers and impacts of the most extreme marine heatwave events. *Scientific Reports*, **10,** 19359.

Shi, J., C. Tang, Q. Liu, Y. Zhang, H. Yang, and C. Li, 2022: Role of Mixed Layer Depth in the Location and Development of the Northeast Pacific Warm Blobs. *Geophysical Research Letters*, **49,** e2022GL098849.

Shin, S. I., P. D. Sardeshmukh, M. Newman, C. Penland, and M. A. Alexander, 2021: Impact of Annual Cycle on ENSO Variability and Predietability. *Journal of Climate*, **34,** 171-193.

Smith, K. E., M. T. Burrows, A. J. Hobday, A. Sen Gupta, P. J. Moore, M. Thomsen, T. Wernberg, and D. A. Smale, 2021: Socioeconomic impacts of marine heatwaves: Global issues and opportunities. *Science*, **374,** eabj3593.

Smith, K. E., and Coauthors, 2023: Biological Impacts of Marine Heatwaves. *Annual Review of Marine Science*, **15,** 119-145.

Smith, T. M., R. W. Reynolds, T. C. Peterson, and J. Lawrimore, 2008: Improvements to NOAA's historical merged land-ocean surface temperature analysis (1880-2006). *Journal of Climate*, **21,** 2283-2296.

Takahashi, N., K. J. Richards, N. Schneider, M. F. Stuecker, H. Annamalai, and M. Nonaka, 2023: Observed Relative Contributions of Anomalous Heat Fluxes and Effective Heat Capacity to Sea Surface Temperature Variability. *Geophysical Research Letters*, **50,** e2023GL103165.

Thompson, C. J., and D. S. Battisti, 2000: A Linear Stochastic Dynamical Model of ENSO. Part I: Model Development. *Journal of Climate*, **13,** 2818-2832.

Vimont, D. J., J. M. Wallace, and D. S. Battisti, 2003: The seasonal footprinting mechanism in the Pacific: Implications for ENSO. *Journal of Climate*, **16,** 2668-2675.

Vimont, D. J., M. A. Alexander, and M. Newman, 2014: Optimal growth of central and east Pacific ENSO events. *Geophysical Research Letters*, **41,** 4027-4034.

Vimont, D. J., M. Newman, D. S. Battisti, and S.-I. Shin, 2022: The Role of Seasonality and the ENSO Mode in Central and East Pacific ENSO Growth and Evolution. *Journal of Climate*, **35,** 3195-3209.

von Storch, H., G. Bürger, R. Schnur, and J.-S. von Storch, 1995: Principal Oscillation Patterns: A Review. *Journal of Climate*, **8,** 377-400.

Wang, C., C. Deser, J.-Y. Yu, P. DiNezio, and A. Clement, 2017: El Niño and Southern Oscillation (ENSO): A Review. *Coral Reefs of the Eastern Tropical Pacific: Persistence and Loss in a Dynamic Environment*, P. W. Glynn, D. P. Manzello, and I. C. Enochs, Eds., Springer Netherlands, 85-106.

Wang, Y., N. J. Holbrook, and J. B. Kajtar, 2023: Predictability of Marine Heatwaves off Western Australia Using a Linear Inverse Model. *Journal of Climate*, **36,** 6177-6193.

Xu, T., M. Newman, A. Capotondi, and E. Di Lorenzo, 2021: The Continuum of Northeast Pacific Marine Heatwaves and Their Relationship to the Tropical Pacific. *Geophysical Research Letters*, **48,** 2020GL090661.

Xu, T., M. Newman, A. Capotondi, S. Stevenson, E. Di Lorenzo, and M. A. Alexander, 2022: An increase in marine heatwaves without significant changes in surface ocean temperature variability. *Nature Communications*, **13,** 7396.

Xue, Y., A. Leetmaa, and M. Ji, 2000: ENSO prediction with Markov models: The impact of sea level. *Journal of Climate*, **13,** 849-871.

Zhang, L., G. Wang, M. Newman, and W. Han, 2021: Interannual to Decadal Variability of Tropical Indian Ocean Sea Surface Temperature: Pacific Influence versus Local Internal Variability. *Journal of Climate*, **34,** 2669-2684.

Zhang, X., F. Li, Z. Jing, B. Zhang, X. Ma, and T. Du, 2024: Detecting marine heatwaves below the sea surface globally using dynamics-guided statistical learning. *Communications Earth & Environment*, **5,** 616.

Zhao, Y., M. Newman, A. Capotondi, E. Di Lorenzo, and D. Sun, 2021: Removing the Effects of Tropical Dynamics from North Pacific Climate Variability. *Journal of Climate***,** 1-49.

Zuo, H., M. A. Balmaseda, S. Tietsche, K. Mogensen, and M. Mayer, 2019: The ECMWF operational ensemble reanalysis–analysis system for ocean and sea ice: a description of the system and assessment. *Ocean Sci.*, **15,** 779-808.